




Article

Interaction of Variable Fluid Properties with Electrokinetically Modulated Peristaltic Flow of Reactive Nanofluid: A Thermodynamical Analysis

Yasir Akbar ^{1,2} , Shiping Huang ^{1,2,*}  and Hammad Alotaibi ³ ¹ China-Singapore International Joint Research Institute, Guangzhou 510700, China² School of Civil Engineering and Transportation, South China University of Technology, Guangzhou 510640, China³ Department of Mathematics and Statistics, College of Science, Taif University, P.O. Box 11099, Taif 21944, Saudi Arabia

* Correspondence: ctasihuang@scut.edu.cn

Abstract: In the present study, the interaction of variable fluid properties with electrokinetically regulated peristaltic transportation of a reactive nanofluid embedded in a porous space is studied. The nanofluid saturates the porous space/medium with inhomogeneous porosity, which changes with distance from the channel boundary. It is assumed that nanofluids are accompanied by variable thermal conductivity and viscosity. The impacts of magnetic field, Brownian motion, electric field, viscous dissipation, chemical reaction, mixed convection, and thermophoresis are incorporated. Moreover, the contribution of zero mass flux boundary condition is executed. The complexity of the equations describing the flow of a nanofluid is reduced by applying the lubrication theory. The fully non-linear equations are solved by utilizing a numerical technique. Particular attention is paid to the analysis of entropy optimization, since its minimization is the best measure to enhance the efficiency of thermal systems. These results demonstrate that a positively oriented external electric field contributes to an increase in nanofluid velocity. Temperature of nanofluid increases more rapidly due to an augmentation in Joule heating parameter. It is noticed that the temperature of water is comparatively lower than that of kerosene. The system's energy loss can be reduced when the thermal conductivity parameter enhance. The magnitude of Bejan number is enhanced by increasing electroosmotic parameter. Further, a substantial decrement in concentration profile is perceived when the Schmidt number is augmented.

Keywords: variable fluid properties; variable porosity; electrokinetic forces; zero mass flux; heat transfer**MSC:** 80A19; 35Q79; 76S05

Citation: Akbar, Y.; Huang, S.; Alotaibi, H. Interaction of Variable Fluid Properties with Electrokinetically Modulated Peristaltic Flow of Reactive Nanofluid: A Thermodynamical Analysis. *Mathematics* **2022**, *10*, 4452. <https://doi.org/10.3390/math10234452>

Academic Editors: Shujin Laima, Yong Cao, Xiaowei Jin and Hehe Ren

Received: 27 October 2022

Accepted: 22 November 2022

Published: 25 November 2022

Publisher's Note: MDPI stays neutral with regard to jurisdictional claims in published maps and institutional affiliations.



Copyright: © 2022 by the authors. Licensee MDPI, Basel, Switzerland. This article is an open access article distributed under the terms and conditions of the Creative Commons Attribution (CC BY) license (<https://creativecommons.org/licenses/by/4.0/>).

1. Introduction

The importance of peristaltic mechanisms in numerous physiological and industrial processes has rendered this concept convincingly trendy in research. Peristaltic motion is a type of wave motion that occurs within tubular systems that spread out along their length. Peristaltic motion is observed in tiny blood vessel vasomotion, bile in the bile duct, valveless movement of the cardiovascular system, transport of cilia etc. This process has crucial functions in the health industry involving noxious fluid transfer, heart lung units, rotary pumps, warm locomotion etc. Engineers used peristaltic activity, which has many industrial applications. Roller and finger motors, in fact, work according to this mechanism. Historically, Latham [1] and Shapiro et al. [2] initially conducted the analysis on peristaltic movement of viscous liquid. They conducted their investigation under creeping flow phenomena. Srinivas et al. [3] presented a thermal analysis with slip conditions on MHD peristaltic motion. Khan et al. [4] illustrated the impacts of magnetic field on Walter's B

liquid through an inclined channel. Impact of heterogeneous-homogeneous reactions on peristaltic movement of Bingham fluid via channel is reported by Tanveer et al. [5].

The rapid progress of nanoscience has revolutionized every area of life, i.e., information technology, energy, food safety, national security, industry, transportation, medicine, and environmental discipline. The use of nanotechnology in medicine/drugs has led to significant improvements through the restructuring of outdated treatments. Nowadays, operations are performed without involving any cuts and prunes for brain tumors, cancer treatment and lithotripsy that were once thought to be incredibly challenging and menacing. Apart from countless applications of nanofluids in industrial and practical settings, the primary goal of nanoparticles is to improve heat transfer phenomena. Choi and Eastman [6,7] were the first who discussed the concept of nanofluids. Shehzad et al. [8] addressed peristaltic transportation of nanoliquid with MHD effects. The numerical results were acquired in this study. Peristaltic transport of ionic nanofluids with double diffusive convection were discussed by Prakash et al. [9]. Recently, analytical results for peristaltic transportation of non-Newtonian Bingham blood liquid via divergent channels were highlighted by Eldabe et al. [10]. Additional research can be seen in references [11–13] on improving heat transmission.

Fluid movement across porous material has been of enormous concern over the last few years owing to its multiple uses in medicine and industry. Flow through porous material takes place in human lungs, rye bread, bile ducts and movement of underground water etc. Fluid flow via porous material has an effective role in the field of food industries, petroleum engineering, biological systems, and hydrology. Such uses can be found in production of oil, fossil fuels, bio films, heat pipes, pebble-type heat exchanger, catalytic reactors, thin glass bead packs etc. The preliminary analysis on porous media was executed by Darcy [14]. An investigation of variants in porous space motion models is presented by Alazmi et al. [15]. A detailed study of fluctuating porosity, local thermal non equilibrium and thermal dispersion on free surface flow in porous space were checked by Alazmi et al. [16]. Pal et al. [17] explored the aspects of radiation and porous space having variable porosity over a vertical plate. Flows of the boundary layer saturated by nanoliquid in a porous space were debated by Kuznetsov et al. [18]. Asghar et al. [19] illustrated both numerical and analytical results for peristaltic transport of mixed convective flows of viscoelastic liquid.

The main requirements of microfluidic systems are efficient pumping, accurate mixing, and flow command. Electroosmotic pumps (EOPs), built on the principle of electroosmosis, are more ordinary micropumps and are controlled by an external electric field adjacent to the liquid-solid interface. Within the charged layer, an electric double layer (EDL) is developed and linked to the outside diffuse layer. The molecules in the scattered area of the EDL migrate when an external force field is applied, leading to mass dislocation of the fluid caused by the density effect, also referred as electroosmotic flow (EOF). This phenomenon informs implementation in medical diagnostic plans, as well as the development of microchips for transporting small volumes and accurately mixing chemicals. Due to the improved electroosmotic layout, instantaneous yield, and large financial advantages, simulation of electroosmotic nanofluid flows has sparked a great deal of interest. Numerous mathematical models consider how fluid flow behaves in diverse geometries [20–25].

The study of entropy generation is extremely important for evaluating the performance of various industrial and engineering systems. The term entropy comes from the Greek letter Entropia, meaning change or transition to it. Entropy computes the quantity of energy in any system that cannot generate any output. The amount of energy produced in any irreversible phase is called entropy generation. The entropy of reversible processes remains unchanged. For irreversible processes, entropy always increases. Entropy is used to improve system performance. Higher entropy production in a system increases irreversibility, which reduces the efficiency of the system. Therefore, machines require a small amount of entropy for better performance. The principle of entropy generation for thermodynamic systems was originally introduced by Bejan [26]. Rashidi et al. [27]

presented the irreversibility rate for peristaltically driven nanoliquid with blood as a base fluid. Recently, Akbar et al. [28] highlighted the aspects of radiative heat flux and Hall currents in peristaltic transportation of nanoliquid with irreversibility rate. Thereafter, many researchers discuss the study of entropy generation for nanoliquids (see refs. [29–31]).

The novelty of the present communication is to study the interaction of variable fluid properties with electrokinetically regulated peristaltic transportation of a reactive nanofluid through an inhomogeneous porous medium. Aspects of variable thermal conductivity, mixed convection, electric field, thermophoresis, variable viscosity, chemical reaction, viscous dissipation, magnetic field, and Brownian movement are brought into contemplation. The mathematical formulation is constructed subject to zero mass flux boundary condition. Numerical results are computed by using NDSolve in Mathematica. Salient properties of different integrated parameters on flow quantities are addressed via graphs and tables.

2. Problem Description

Here we considered the 2D peristaltic carriage of an aqueous solution, which varies through an external electric field along the length of the channel. The combined effects of peristaltic pumping and applied electric field cause fluid to flow in a symmetric channel. The process of peristalsis occurs because sinusoidal waves passing along the channel boundaries with a constant velocity c . The surface of the channel barrier develops a negative charge as a result of the ions present in the fluid medium, pulling counterions to it. This produces an EDL, a layer of counterions close to the channel boundary. The counterions in the EDL migrate towards their respective electrodes when an electrical source is provided through the channel’s ends, exerting a driving force on the liquid particles. Further, it is supposed that the electric field E_x has imposed axially, and magnetic field B_0 is transversely of the fluid flow. The geometry of the problem is presented via Figure 1. Mathematically, the boundaries of the channel walls are described as [8]:

$$\pm H(\bar{X}, \bar{t}) = \pm a_1 \cos\left(\frac{2\pi}{\lambda}(\bar{X} - c\bar{t})\right) \pm d_1. \tag{1}$$

Here d_1 and λ are respectively the half width of the channel and wavelength. The function of the electric potential in the electrolyte satisfies the Poisson equation. In accordance with it, the electric potential Ω is expressed as [20]:

$$\nabla^2 \Omega = -\frac{\rho_e}{\epsilon}. \tag{2}$$

where ρ_e is the net charge density of the mixture at present and is defined as:

$$\rho_e = ez(\bar{n}_+ - \bar{n}_-). \tag{3}$$

The Boltzmann distribution function for local ionic density is given as:

$$\bar{n}_\pm = \bar{n}_0 e^{\left(\pm \frac{ez}{T_{av} k_B} \Omega\right)}. \tag{4}$$

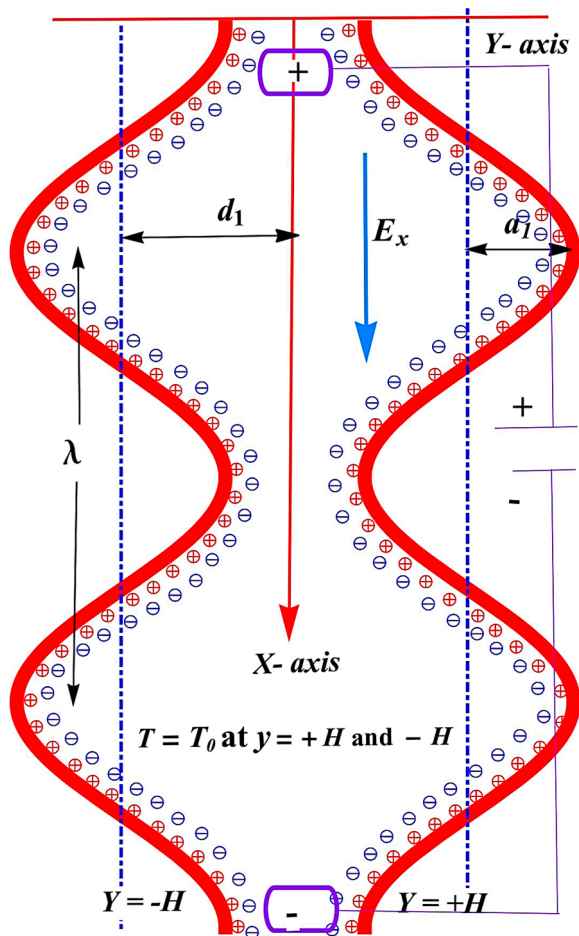


Figure 1. Geometric representation of the problem.

Three important aspects are considered here: convection, diffusion, and chemical reaction. The diffusion-convection reaction illustrates how these three mechanisms affect a substance’s concentration as it is dispersed throughout a medium. Numerous industrial applications exist for reactive convective diffusion. The variable viscosity, porosity, and thermal conductivity (changeable liquid characteristics) of the fluid are considered in the analysis. Further, the aspects of mixed convection, electric field, thermophoresis, viscous dissipation, magnetic field, chemical reaction, and Brownian movement are carried out. Utilizing the Oberbeck-Boussinesq approximation and considering the most suitable practical case when the concentration of nanoparticles is diluted, and choosing an appropriate reference pressure, the basic governing equations are specified as [11,22,29,31]:

$$\frac{\partial \bar{U}}{\partial \bar{X}} + \frac{\partial \bar{V}}{\partial \bar{Y}} = 0, \tag{5}$$

$$\rho_f \left(\frac{\partial \bar{U}}{\partial \bar{t}} + \bar{U} \frac{\partial \bar{U}}{\partial \bar{X}} + \bar{V} \frac{\partial \bar{U}}{\partial \bar{Y}} \right) = - \frac{\partial \bar{P}}{\partial \bar{X}} + \frac{\partial}{\partial \bar{Y}} \left[\mu_f(T) \left(\frac{\partial \bar{U}}{\partial \bar{Y}} + \frac{\partial \bar{V}}{\partial \bar{X}} \right) \right] + 2 \frac{\partial}{\partial \bar{X}} \left[\mu_f(T) \frac{\partial \bar{U}}{\partial \bar{X}} \right] - \bar{U} B_0^2 \sigma_f + \frac{\mu_f(T)}{k_1(\bar{Y})} \bar{U} + \alpha \rho_f g (T - T_0) + \alpha^* \rho_f g (C - C_0) + \rho_e E_x, \tag{6}$$

$$\rho_f \left(\frac{\partial \bar{V}}{\partial \bar{t}} + \bar{U} \frac{\partial \bar{V}}{\partial \bar{X}} + \bar{V} \frac{\partial \bar{V}}{\partial \bar{Y}} \right) = - \frac{\partial \bar{P}}{\partial \bar{Y}} + \frac{\partial}{\partial \bar{X}} \left[\mu_f(T) \left(\frac{\partial \bar{V}}{\partial \bar{X}} + \frac{\partial \bar{U}}{\partial \bar{Y}} \right) \right] + 2 \frac{\partial}{\partial \bar{Y}} \left[\mu_f(T) \frac{\partial \bar{V}}{\partial \bar{Y}} \right] + \frac{\mu_f(T)}{k_1(\bar{Y})} \bar{V} + E_x B_0 \sigma_f, \tag{7}$$

$$\begin{aligned}
 (\rho C)_f \left(\bar{U} \frac{\partial T}{\partial \bar{X}} + \bar{V} \frac{\partial T}{\partial \bar{Y}} + \frac{\partial T}{\partial \bar{t}} \right) &= \left(\frac{\partial T}{\partial \bar{Y}} + \frac{\partial T}{\partial \bar{X}} \right) \left[K_f(T) \left(\frac{\partial T}{\partial \bar{X}} + \frac{\partial T}{\partial \bar{Y}} \right) \right] + \frac{\mu_f(T)}{\tilde{k}_1(\bar{Y})} (\bar{V}^2 + \bar{U}^2) + \sigma_f B_0^2 \bar{U}^2 \\
 &+ \tau(\rho C)_f \left[\frac{D_T}{T_m} \left\{ \left(\frac{\partial T}{\partial \bar{X}} \right) + \left(\frac{\partial T}{\partial \bar{Y}} \right) \right\}^2 + D_B \left(\frac{\partial T}{\partial \bar{X}} \frac{\partial C}{\partial \bar{X}} + \frac{\partial C}{\partial \bar{Y}} \frac{\partial T}{\partial \bar{Y}} \right) \right] \\
 &+ \mu_f(T) \left[\left(\frac{\partial \bar{V}}{\partial \bar{X}} + \frac{\partial \bar{U}}{\partial \bar{Y}} \right)^2 + 2 \left(\frac{\partial \bar{U}}{\partial \bar{X}} \right)^2 + 2 \left(\frac{\partial \bar{V}}{\partial \bar{Y}} \right)^2 \right] + \sigma_f (E_x)^2,
 \end{aligned} \tag{8}$$

$$\left(\frac{\partial C}{\partial \bar{t}} + \bar{U} \frac{\partial C}{\partial \bar{X}} + \bar{V} \frac{\partial C}{\partial \bar{Y}} \right) = D_B \left(\frac{\partial^2 C}{\partial \bar{Y}^2} + \frac{\partial^2 C}{\partial \bar{X}^2} \right) + \frac{D_T}{T_m} \left(\frac{\partial^2 T}{\partial \bar{X}^2} + \frac{\partial^2 T}{\partial \bar{Y}^2} \right) - \widehat{\gamma}_c (C - C_0). \tag{9}$$

where $\bar{P}(\bar{X}, \bar{Y}, \bar{t})$, T , ρ_f and K_f are the pressure, temperature, density, and thermal conductivity, respectively. Fixed frame to wave frame transformation is described as [22]:

$$\bar{x} = \bar{X} - c\bar{t}, \bar{v}(\bar{x}, \bar{y}) = \bar{V}(\bar{X}, \bar{t}, \bar{Y}), \bar{p}(\bar{x}, \bar{y}) = \bar{P}(\bar{X}, \bar{t}, \bar{Y}), \bar{u}(\bar{x}, \bar{y}) = \bar{U}(\bar{Y}, \bar{t}, \bar{X}) - c. \tag{10}$$

In wave frame, Equations (5)–(9) become:

$$\frac{\partial \bar{u}}{\partial \bar{x}} + \frac{\partial \bar{v}}{\partial \bar{y}} = 0, \tag{11}$$

$$\begin{aligned}
 \rho_f \left((c + \bar{u}) \frac{\partial \bar{u}}{\partial \bar{x}} + \bar{v} \frac{\partial \bar{u}}{\partial \bar{y}} \right) &= -\frac{\partial \bar{P}}{\partial \bar{x}} + \frac{\partial}{\partial \bar{y}} \left[\mu_f(T) \left\{ \frac{\partial \bar{v}}{\partial \bar{x}} + \frac{\partial \bar{u}}{\partial \bar{y}} \right\} \right] + 2 \frac{\partial}{\partial \bar{x}} \left[\mu_f(T) \frac{\partial \bar{u}}{\partial \bar{x}} \right] - (\bar{u} + c) B_0^2 \sigma_f \\
 &+ \frac{\mu_f(T)}{\tilde{k}_1(\bar{y})} \bar{U} + g(T - T_0) \alpha \rho_f + \rho_f \alpha^* g(C - C_0) + \rho_e E_x,
 \end{aligned} \tag{12}$$

$$\begin{aligned}
 \rho_f \left((\bar{u} + c) \frac{\partial \bar{v}}{\partial \bar{x}} + \bar{v} \frac{\partial \bar{v}}{\partial \bar{y}} \right) &= -\frac{\partial \bar{P}}{\partial \bar{y}} + \frac{\partial}{\partial \bar{x}} \left[\mu_f(T) \left\{ \frac{\partial \bar{v}}{\partial \bar{x}} + \frac{\partial \bar{u}}{\partial \bar{y}} \right\} \right] + 2 \frac{\partial}{\partial \bar{y}} \left[\mu_f(T) \frac{\partial \bar{v}}{\partial \bar{y}} \right] \\
 &+ \frac{\mu_f(T)}{\tilde{k}_1(\bar{y})} \bar{v} + E_x B_0 \sigma_f,
 \end{aligned} \tag{13}$$

$$\begin{aligned}
 (\rho C)_f \left((\bar{u} + c) \frac{\partial T}{\partial \bar{x}} + \bar{v} \frac{\partial T}{\partial \bar{y}} \right) &= \left(\frac{\partial T}{\partial \bar{y}} + \frac{\partial T}{\partial \bar{x}} \right) \left[K_f(T) \left(\frac{\partial T}{\partial \bar{y}} + \frac{\partial T}{\partial \bar{x}} \right) \right] + \frac{\mu_f(T)}{\tilde{k}_1(\bar{y})} ((\bar{u} + c)^2 + \bar{v}^2) + \sigma_f B_0^2 \bar{U}^2 \\
 &+ \tau(\rho C)_f \left[\frac{D_T}{T_m} \left\{ \left(\frac{\partial T}{\partial \bar{x}} \right) + \left(\frac{\partial T}{\partial \bar{y}} \right) \right\}^2 + D_B \left(\frac{\partial C}{\partial \bar{x}} \frac{\partial T}{\partial \bar{x}} + \frac{\partial C}{\partial \bar{y}} \frac{\partial T}{\partial \bar{y}} \right) \right] \\
 &+ \mu_f(T) \left[\left(\frac{\partial \bar{v}}{\partial \bar{x}} + \frac{\partial \bar{u}}{\partial \bar{y}} \right)^2 + 2 \left(\frac{\partial \bar{u}}{\partial \bar{x}} \right)^2 + 2 \left(\frac{\partial \bar{v}}{\partial \bar{y}} \right)^2 \right] + \sigma_f (E_x)^2,
 \end{aligned} \tag{14}$$

$$\left(\bar{v} \frac{\partial C}{\partial \bar{y}} + (\bar{u} + c) \frac{\partial C}{\partial \bar{x}} \right) = D_B \left(\frac{\partial^2 C}{\partial \bar{y}^2} + \frac{\partial^2 C}{\partial \bar{x}^2} \right) + \frac{D_T}{T_m} \left(\frac{\partial^2 T}{\partial \bar{x}^2} + \frac{\partial^2 T}{\partial \bar{y}^2} \right) - \widehat{\gamma}_c (C - C_0). \tag{15}$$

Reynold’s model of viscosity was intimated as a [29]:

$$\mu_f(T) = \mu_0 e^{-\alpha_0(T - T_0)}, \text{ for } \alpha_0 \ll 1, \tag{16}$$

which, after performing Maclaurin’s series, can be recorded as:

$$\mu_f(T) = \mu_0 (1 - \alpha_0(T - T_0)), \text{ for } \alpha_0 \ll 1, \tag{17}$$

where α_0 is the dimensional viscosity parameter. Further, the temperature-depending thermal conductivity [31] is classified as:

$$K_f(T) = K_0 (1 + \xi_0(T - T_0)), \tag{18}$$

where ξ_0 is the dimensional thermal conductivity parameter.

Equations (3) and (4) in (2) and the Debye-Hückel estimation [21]:

$$\frac{d^2\Omega}{dy^2} = \omega^2\Omega. \tag{19}$$

Equation (19) is subject to the assumption that the potential is fixed at the wall surface and that the potential distribution is symmetrical about the center line.

$$\begin{aligned} \Omega(y) &= 1, \text{ at } y = h, \\ \Omega'(y) &= 0, \text{ at } y = 0. \end{aligned} \tag{20}$$

where the electroosmotic parameter is represented by ω . It is given as:

$$\omega = \frac{d}{\lambda_D}, \tag{21}$$

where,

$$\lambda_D = \frac{1}{ez} \left(\frac{\epsilon K_B T_{av}}{2n_0} \right)^{\frac{1}{2}}. \tag{22}$$

The potential function is calculated from Equation (19) subject to boundary conditions (20) in the following manner:

$$\Omega(y) = \frac{\cosh(\omega y)}{\cosh(\omega h)}. \tag{23}$$

In view of “low Reynolds and long wavelength approximations”, Equations (12)–(15) become:

$$0 = -\frac{\partial p}{\partial x} + \frac{\partial}{\partial y} \left((1 - \alpha\theta) \frac{\partial^2 \psi}{\partial y^2} \right) + G_t \theta + G_c \phi - M^2 \left(1 + \frac{\partial \psi}{\partial y} \right) + \frac{1}{k(y)} \left(\frac{\partial \psi}{\partial y} + 1 \right) + U_{hs} \Omega''(y), \tag{24}$$

$$0 = \frac{\partial p}{\partial y}, \tag{25}$$

$$\begin{aligned} 0 &= \frac{\partial}{\partial y} \left[(1 + \zeta\theta) \frac{\partial \theta}{\partial y} \right] + Br(1 - \alpha\theta) \left(\frac{\partial^2 \psi}{\partial y^2} \right)^2 + BrM^2 \left(1 + \frac{\partial \psi}{\partial y} \right)^2 + S + PrN_b \left(\frac{\partial \theta}{\partial y} \frac{\partial \phi}{\partial y} \right) \\ &+ \frac{Br(1 - \alpha\theta)}{k(y)} \left(\frac{\partial \psi}{\partial y} + 1 \right)^2 + PrN_t \left(\frac{\partial \theta}{\partial y} \right)^2, \end{aligned} \tag{26}$$

$$0 = \frac{\partial^2 \phi}{\partial y^2} + \frac{N_t}{N_b} \left(\frac{\partial^2 \theta}{\partial y^2} \right) - S_c \gamma_c \phi. \tag{27}$$

The non-dimensional quantities used in the aforementioned calculations are:

$$\begin{aligned} x &= \frac{\bar{x}}{\lambda}, \quad t = \frac{c\bar{t}}{\lambda}, \quad h = \frac{\bar{H}_1}{d_1}, \quad a = \frac{a_1}{d_1}, \quad p = \frac{d_1^2 \bar{p}}{c\lambda\mu_0}, \quad v = \frac{\mu_0}{\rho_f}, \quad y = \frac{\bar{y}}{d_1}, \quad v = \frac{\bar{v}}{c\delta}, \quad \delta = \frac{d_1}{\lambda}, \quad \zeta = \zeta_0 T_0, \\ K(\theta) &= \frac{\bar{K}(T)}{K_0}, \quad M^2 = \frac{\sigma_f}{\mu_0} B_0^2 d_1^2, \quad u = \frac{\bar{u}}{c}, \quad Re = \frac{\rho_f c d_1}{\mu_0}, \quad Pr = \frac{\mu_0 C_f}{K_0}, \quad Ec = \frac{c^2}{C_f T_0}, \quad \alpha = \alpha_0 T_0 \\ \phi &= \frac{C - C_0}{C_0}, \quad \theta = \frac{T - T_0}{T_0}, \quad Br = Pr.Ec, \quad N_t = \frac{\tau D_T T_0}{v T_m}, \quad N_b = \frac{\tau D_B C_0}{v}, \quad S = \frac{d_1^2 \sigma_f E_x^2}{K_0 T_0}, \quad v = -\psi_x, \\ S_c &= \frac{\mu_0}{\rho_f D_B}, \quad G_t = \frac{\rho_f g \alpha d_1^2 T_0}{\mu_0 c}, \quad G_c = \frac{\rho_f g \alpha^* d_1^2 C_0}{\mu_0 c}, \quad u = \psi_y, \quad U_{hs} = -\frac{\epsilon E_x}{\mu_0 c}, \quad \gamma_c = \frac{\hat{\gamma}_c d_1^2}{v}, \\ k(y) &= \frac{\tilde{k}_1(\bar{y})}{d_1^2}. \end{aligned} \tag{28}$$

Also, the continuity Equation (11) is identically satisfied. In given equations, Re , Ec , θ , Pr , M , G_c , U_{hs} , S , γ_c , N_t , S_c , G_t and N_b are the dimensionless Reynolds number, Eckert number, temperature, Prandtl number, Hartman number, concentration Grashoff number, Helmholtz–Smoluchowski velocity, Joule heating parameter, chemical reaction parameter,

thermophoresis parameter, Schmidt number, thermal Grashoff number and Brownian motion parameter, respectively.

The relation between porosity and permeability is given as [11]:

$$k(y) = \frac{d_p^2 \zeta^2}{150(1 - \zeta)^2}. \tag{29}$$

where d_p is the diameter of the pore. Alazmi and Wafai [15,16] showed that porosity depends on the normal distance from the boundary, given as:

$$\zeta = C_0 \left(1 + C_1 \exp\left(-\frac{C_2 y}{d_p}\right) \right). \tag{30}$$

The values of C_1 , C_2 , and C_0 are respectively chosen to be 1, 2 and 0.37 [11]. The mean flows η and F in laboratory and wave frames are defined as:

$$\eta = F + 1. \tag{31}$$

Kuznetsov and Nield [18] suggested that it is more appropriate to take thermophoresis at the boundaries instead of assessing constant nanomaterials concentration at the walls. Mathematically it is defined as:

$$D_B \frac{\partial C}{\partial \bar{Y}} + \frac{D_T}{T_m} \frac{\partial T}{\partial \bar{Y}} = 0, \text{ at } \bar{Y} = \pm H. \tag{32}$$

The dimensionless boundary conditions in moving frame are:

$$\begin{aligned} \psi = 0, \frac{\partial^2 \psi}{\partial y^2} = 0, \frac{\partial \theta}{\partial y} = 0, \frac{\partial \phi}{\partial y} = 0 \quad \text{at } y = 0, \\ \psi = F, \frac{\partial \psi}{\partial y} = -1, \theta = 0, N_b \frac{\partial \phi}{\partial y} + N_t \frac{\partial \theta}{\partial y} = 0 \quad \text{at } y = h. \end{aligned} \tag{33}$$

3. Entropy Generation

It is well known from thermodynamics that the loss of energy in a system contributes to thermodynamic irreversibility, and this produces entropy. Entropy generation is a degree of chaos in a thermodynamic system. In the present study, entropy production comes from various sources such as viscous dissipation, variable porosity, diffusion and EMHD irreversibility. The strength of entropy production (N_S) is defined as:

$$\begin{aligned} N_S = & (1 + \zeta\theta) \left(\frac{\partial \theta}{\partial y}\right)^2 + Br(1 - \alpha\theta) \left(\frac{\partial^2 \psi}{\partial y^2}\right)^2 + BrM^2 \left(1 + \frac{\partial \psi}{\partial y}\right)^2 + S + PrN_b \left(\frac{\partial \theta}{\partial y} \frac{\partial \phi}{\partial y}\right) \\ & + \frac{Br(1 - \alpha\theta)}{k(y)} \left(1 + \frac{\partial \psi}{\partial y}\right)^2 + PrN_t \left(\frac{\partial \theta}{\partial y}\right)^2. \end{aligned} \tag{34}$$

Bejan number is assigned as the proportion of entropy produced by thermal irreversibility to total entropy:

$$B_e = \frac{(1 + \zeta\theta) \left(\frac{\partial \theta}{\partial y}\right)^2}{\left[(1 + \zeta\theta) \left(\frac{\partial \theta}{\partial y}\right)^2 + Br(1 - \alpha\theta) \left(\frac{\partial^2 \psi}{\partial y^2}\right)^2 + BrM^2 \left(1 + \frac{\partial \psi}{\partial y}\right)^2 + S + PrN_b \left(\frac{\partial \theta}{\partial y} \frac{\partial \phi}{\partial y}\right) + \frac{Br(1 - \alpha\theta)}{k(y)} \left(1 + \frac{\partial \psi}{\partial y}\right)^2 + PrN_t \left(\frac{\partial \theta}{\partial y}\right)^2 \right]}. \tag{35}$$

The Bejan number (B_e) is a parameter that reflects the significance of thermal irreversibility in the domain.

The analytical solution of the Equations (24)–(27) in these settings is not an easy job. Findings are graphically interpreted in the next segment. Therefore, the set of differential Equations (24)–(27) subject to boundary conditions (33) are numerically resolved by utilizing NDSolve in Mathematica 13.1. This approach is very effective and beneficial for boundary value problems. Additionally, a step size of 0.01 allows for consistent adjustments of both x and y . The accuracy of this methodology is remarkable and is stable unconditionally.

4. Results and Discussion

Numerical findings are discussed in this section. Graphs for heat transfer, irreversibility rate, Bejan number, concentration and velocity profiles are gained and evaluated. Numerical values of HMT rate at the boundary are displayed via tables.

4.1. Temperature Profile

Figure 2a–f are devoted to estimate the alteration in temperature profile subject to variation in S , ω , N_t , N_b , ξ , and M . Figure 2a reports that temperature profile becomes higher by enhancing S . An electrolyte solution’s resistance to the flow of an electric current is measured by the Joule heating parameter. When S is high, heat production increases as a result of the extraordinarily high drag forces. From Figure 2b, temperature is larger and more progressive on increasing the electroosmotic parameter. Figure 2b reflects that the stronger ω raises the nanofluid temperature. This behavior is expected because higher values of ω cause a thin EDL, so the mass of the liquid proceeds toward the central part of the pump, which raises the temperature of the nanofluid due to significant convection. Figure 2c displays that temperature increases by enhancing the values of N_t . Similarly, an expansion in nanofluid temperature is seen by expanding the values of N_b (see Figure 2d). This is mainly because an improvement in Brownian motion parameter enhances the kinetic energy that converts into internal energy and thereby improves the temperature. A similar inclination was uncovered by Shehzad et al. [8]. Figure 2e shows that the temperature declines by increasing the thermal conductivity parameter. However, a maximum temperature is obtained for constant thermal conductivity. The reason for this is that the liquid’s capability to retain or radiate heat to its vicinity can be regulated by a fluid’s thermal conductivity. When ξ increases, the thermal conductivity of the system is also growing. Therefore, the temperature profile declines. Figure 2f portrays that a stronger magnetic field significantly raises the temperature of nanofluid. This is due to the Joule heating effects. Figure 2g is outlined to assess and measure the temperature of different basic fluids (water and kerosene). It is noticed that the temperature of water is comparatively lower than that of kerosene.

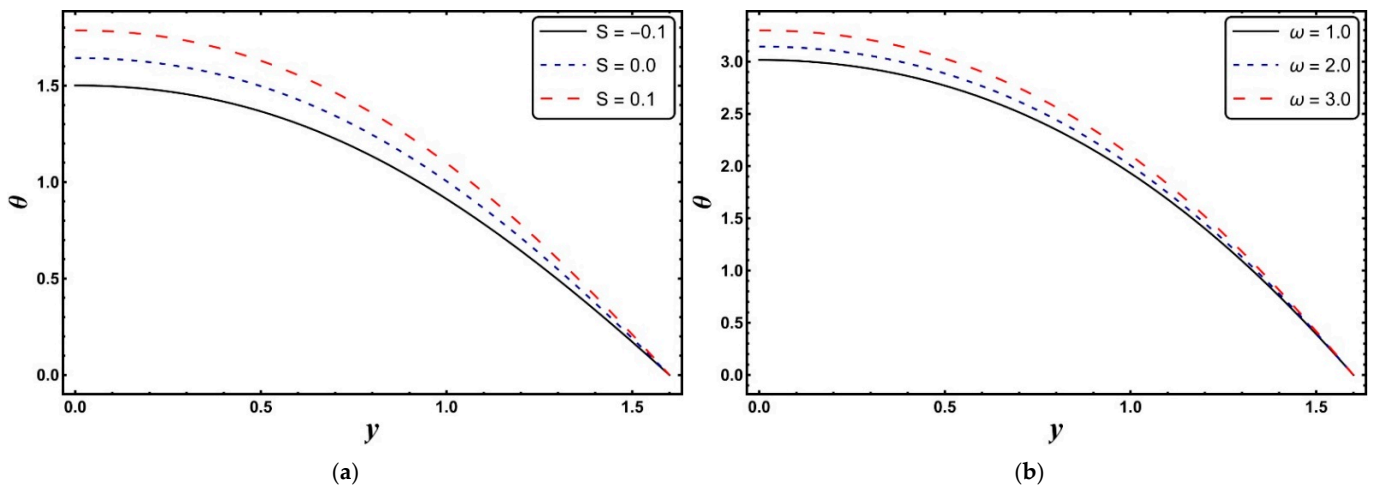


Figure 2. Cont.

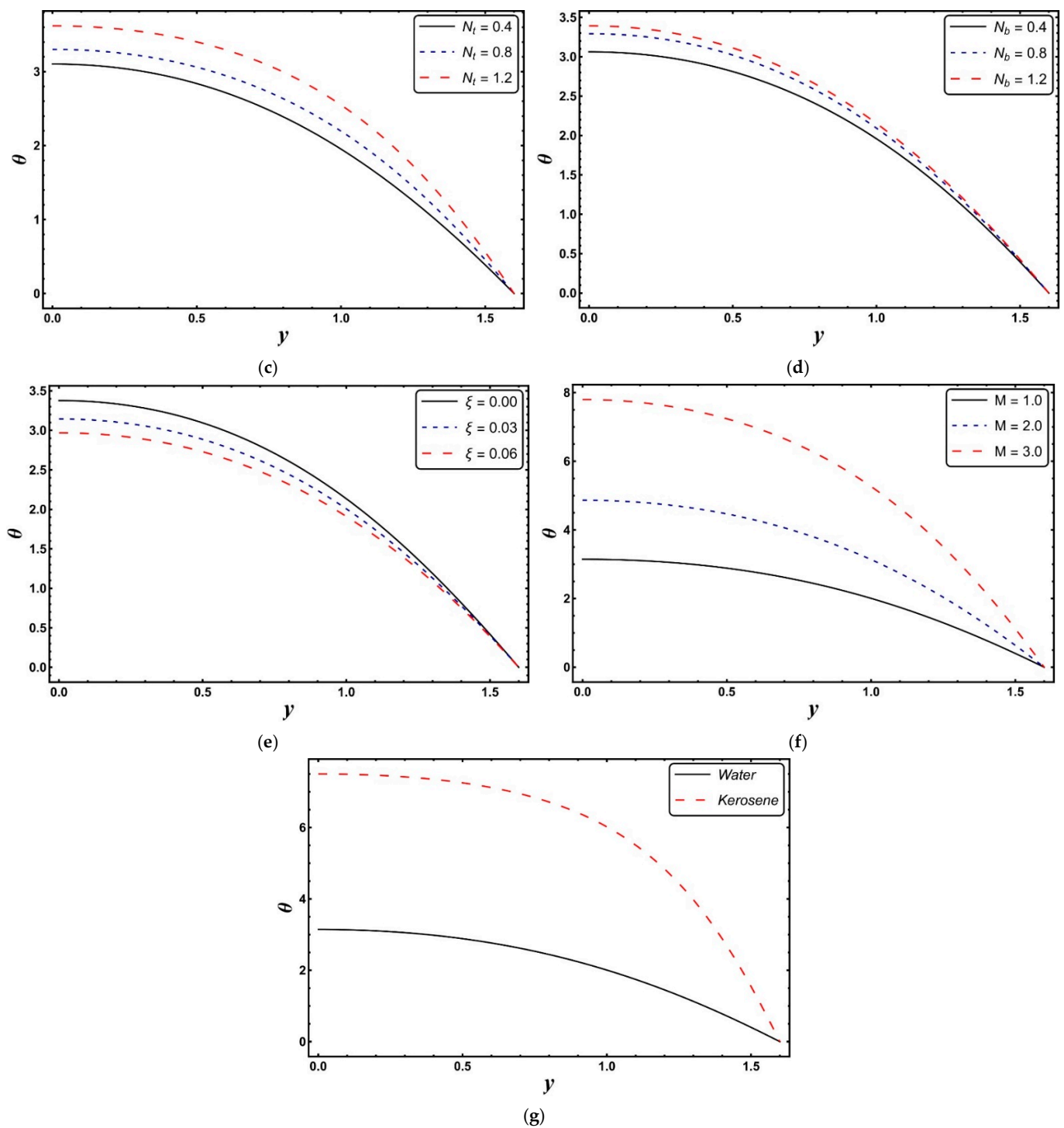
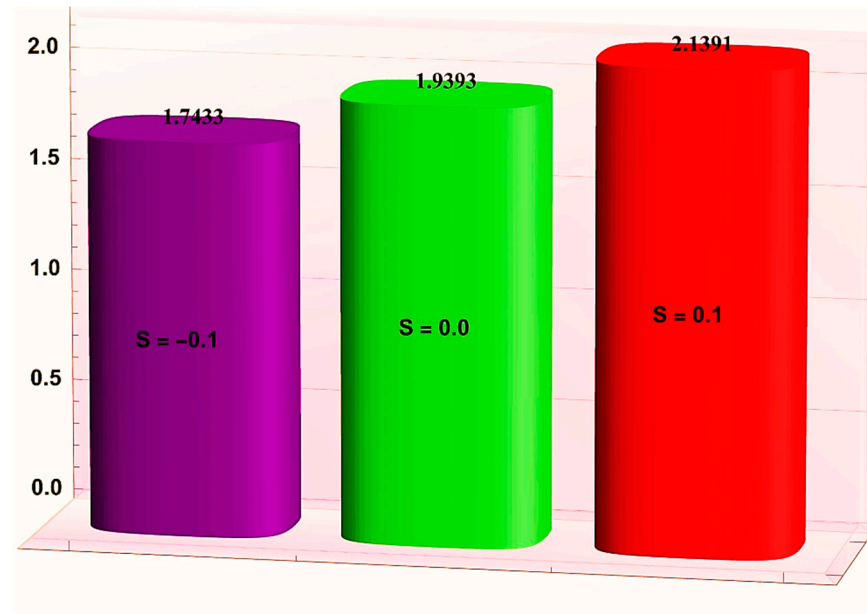


Figure 2. (a–g): Temperature profile against different parameters.

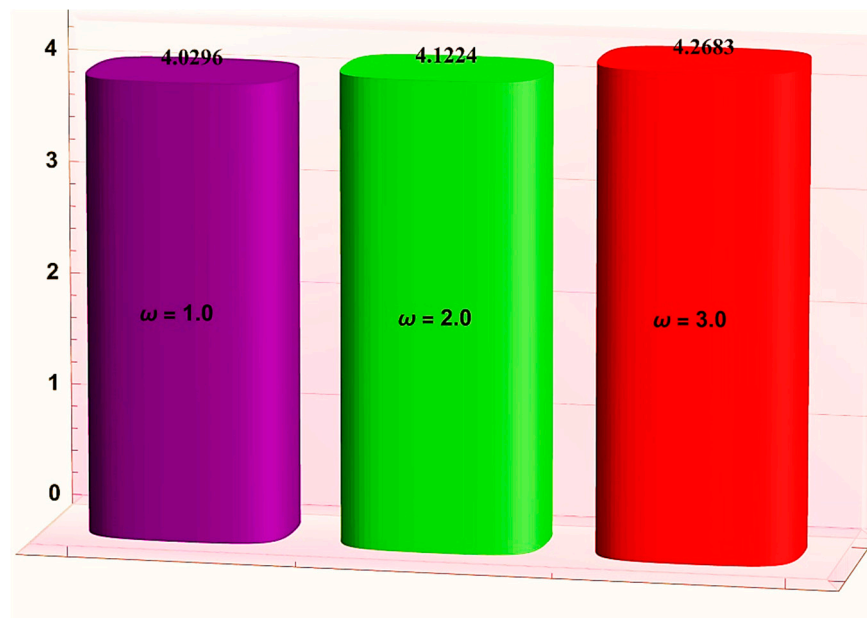
4.2. Heat Transfer Rate at the Wall

Bar charts in Figure 3a–d are prepared to examine the behavior of rate of heat transfer at the wall $-\theta'(h)$ versus various flow parameters. Bar chart in Figure 3a reflects that addition in S develops the $\theta'(h)$. S is related to a square of solidity of the electric field, so an expansion in S is physically correlated with an intense electric field, which in turn accelerates fluids faster and improves convective heat transmission. Therefore, there is a notable increase in the rate of heat transfer. ω with it rising values raises the heat transfer rate (see bar chart in Figure 3b). Since the electroosmotic parameter is inversely proportional to the Debye length, an augmentation in electroosmotic factor reduces the characteristic

Debye length, which results in a growth of $-\theta'(h)$. A similar effect was documented in the research of Hussain et al. [25]. However, the situation is reversed for ξ . From bar chart in Figure 3c, a reduction in $-\theta'(h)$ is witnessed by increasing ξ . Bar chart in Figure 3d exhibits that heat transfer rate significantly improves for higher M . Figure 3e is acquired to measure $-\theta'(h)$ for two different base liquids (kerosene and water). It is assessed that an excessive value of $-\theta'(h)$ is achieved by kerosene as compared to water.

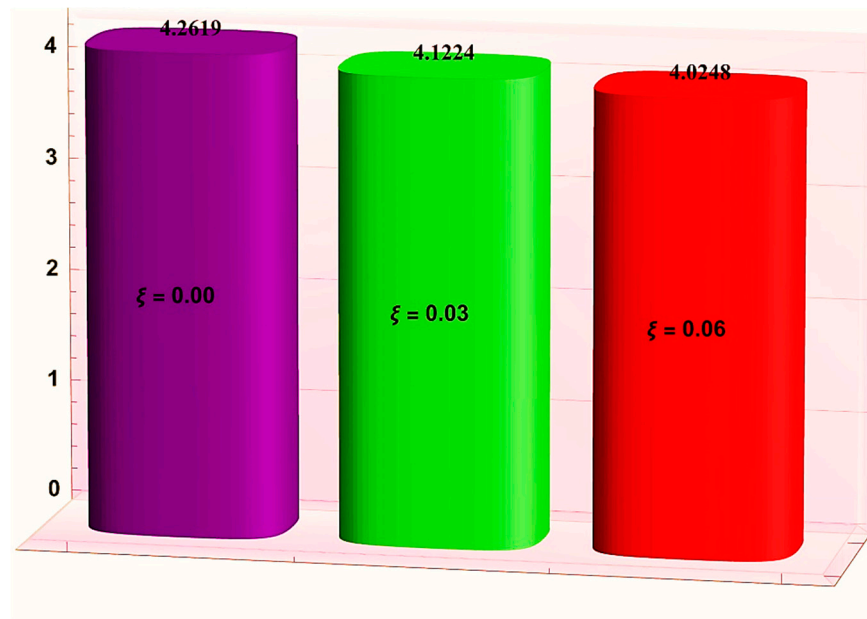


(a)

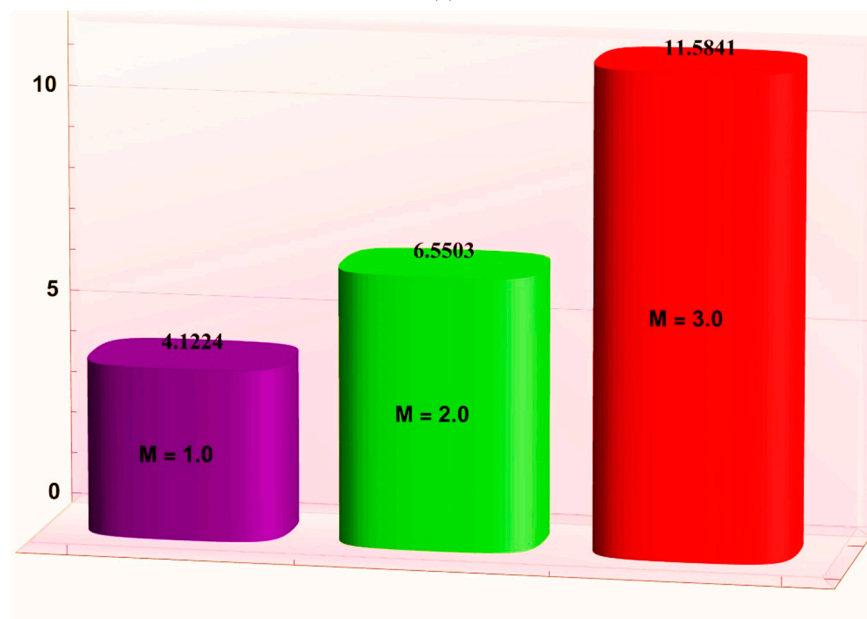


(b)

Figure 3. Cont.

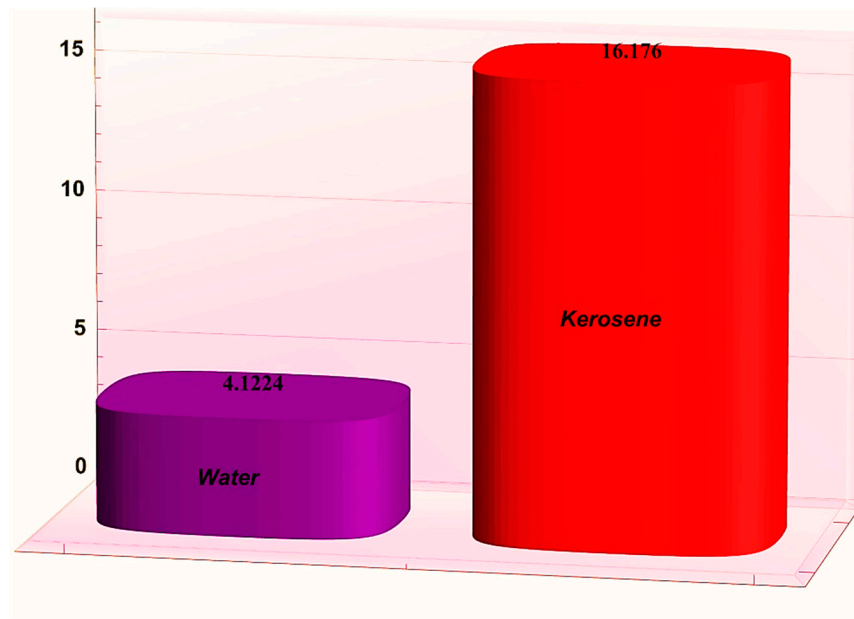


(c)



(d)

Figure 3. Cont.



(e)

Figure 3. (a–e): Effects of different relevant parameters on heat transfer rate at the channel wall $-\theta'(h)$.

4.3. Entropy Analysis

The physical impacts of S , ω , ξ and G_t on entropy generation number (N_s) are shown through Figure 4a–d. Notably, the entropy generation curves exhibit a parabolic tendency with the lowest value close to the channel’s center. The involvement of a Joule heating parameter further amplified the irreversibility process (see Figure 4a). Nanofluid temperature is high due to Joule heating parameter, and then the entropy also increases. This is consistent with the results of Akbar and Alotaibi [22]. It can be perceived from a Figure 4b that an augmentation in the electroosmotic parameter causes a notable increase in entropy generation. Figure 4c elucidates that entropy generation suppresses for higher ξ . Since a larger amount of ξ led to a reduction in temperature and, consequently, less disturbance. From this analysis, we conclude that for thermal management of biomedical instruments, the variable thermal conductivity must be taken into consideration. However, a reverse fashion is detected for larger G_t (see Figure 4d). The process of irreversibility is even more intensified in the presence of mixed convection.

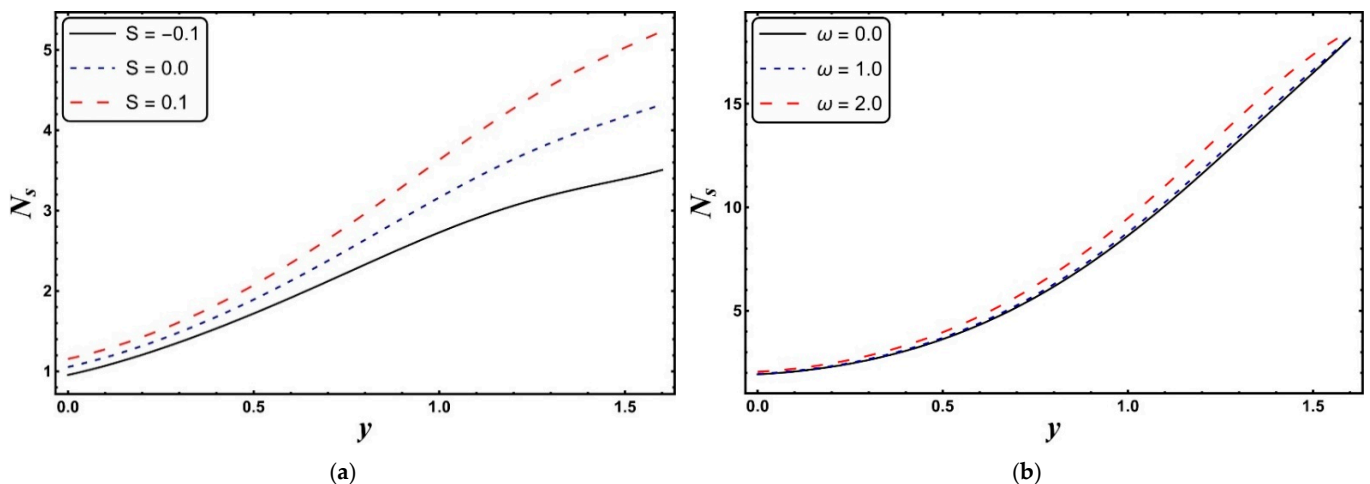


Figure 4. Cont.

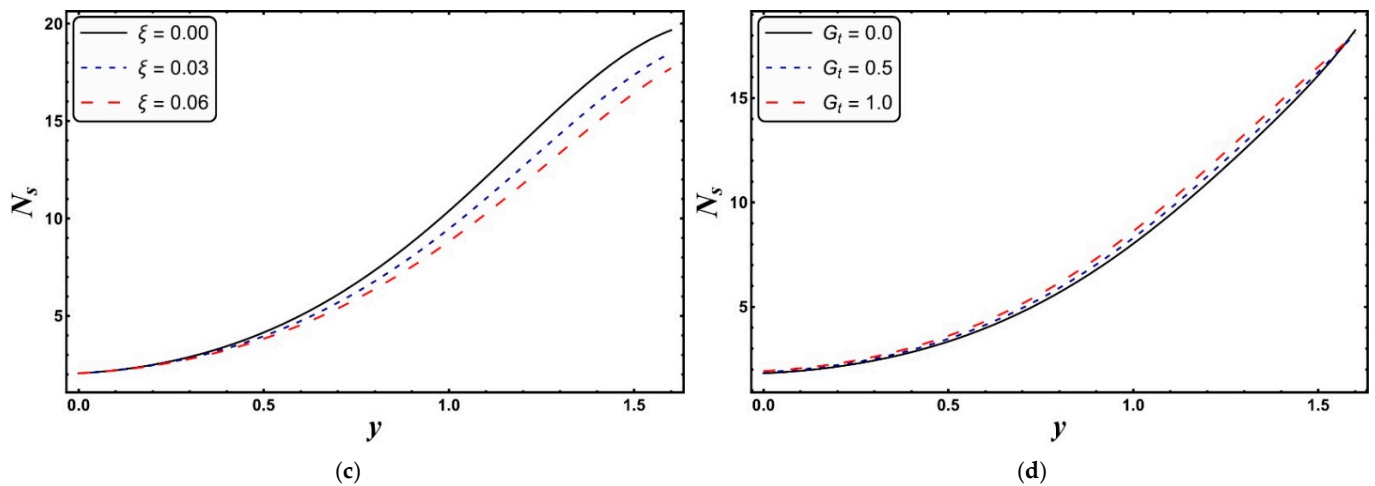


Figure 4. (a–d): Effects of different relevant parameters on entropy generation.

4.4. Bejan Number

Figure 5a–c gives the effects of S , ω and ξ on Bejan number (B_e). In all plots, Bejan number has a supreme value at the wall of the channel ($y = h$). The interval of B_e lies between 0 and 1. In certain cases, if $B_e \rightarrow 1$, in physical terms it indicates that the entropy generation due to heat conduction (HE) is much greater than total entropy generation (TE). While, $B_e \rightarrow 0$, this represents that HE is much less than TE. Figure 5a reflects that the strength of Bejan number is intensified by highlighting S . An increase in S reduces the overall irreversibility, which leads to an increase in the Bejan number. Analogous behavior is also encountered for greater ω . Figure 5c expresses that by mounting the thermal conductivity parameter, Bejan number is weakening.

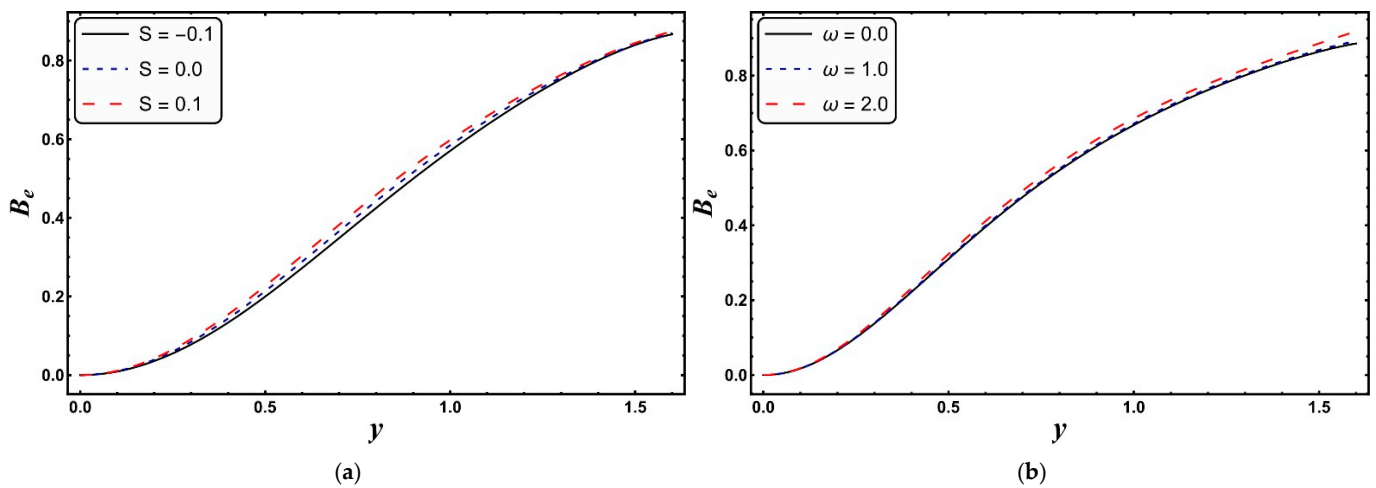


Figure 5. Cont.

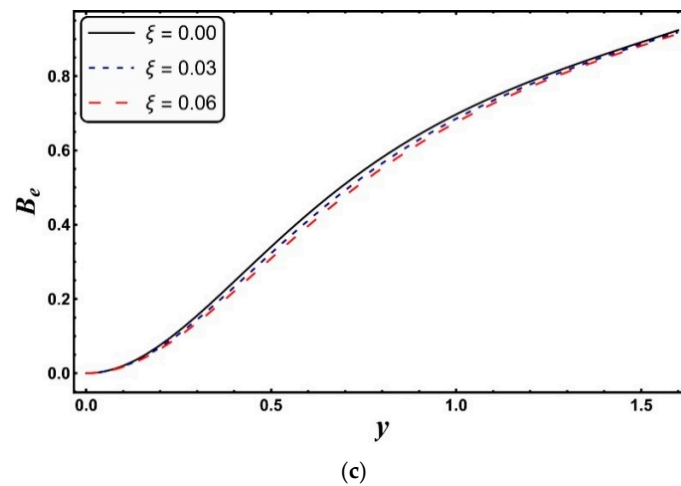


Figure 5. (a–c): Effects of different relevant parameters on Bejan number.

4.5. Nanoparticles Concentration

Impacts of S_c , γ , N_t and N_b on nanoparticles concentration are examined through Figure 6a–d. The resulting sketches manifest that the concentration profile near the walls of the channel is influenced by the parameters contained in the transition. This is primarily due to zero mass flux conditions for the concentration being regarded. Figure 6a portrays that nanoparticles concentration suppresses for larger S_c . Since S_c is inversely proportional to mass diffusion, therefore higher S_c causes a decrease in the mass diffusion rate, which ultimately reduces the concentration of nanoparticles. Figure 6b articulates that nanoparticles concentration is reduced for larger γ . Physical support is provided by the fact that the interfacial mass transfer rate is consolidated as a result of γ , which lowers the concentration profile. Figure 6c describes that a substantial decrease in concentration profile is perceived when N_t is being augmented. Figure 6d indicates that the concentration rises through improved values of N_b . However, the situation is reversed near the channel wall. The progression of N_b enhances the random motion of nanomaterials, which leads to an elevated concentration of nanomaterials.

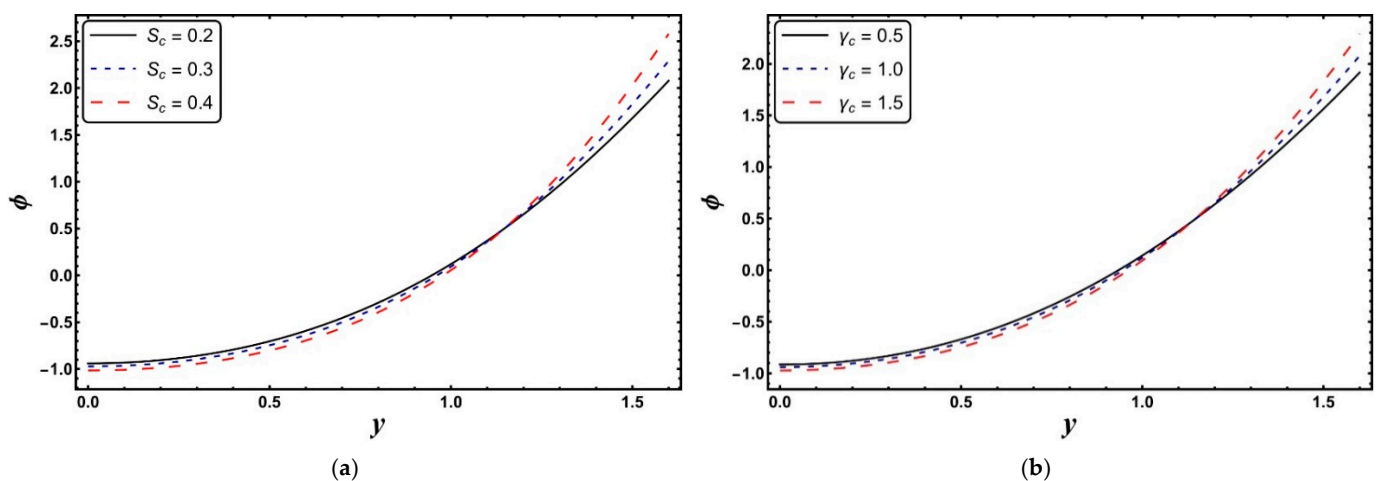


Figure 6. Cont.

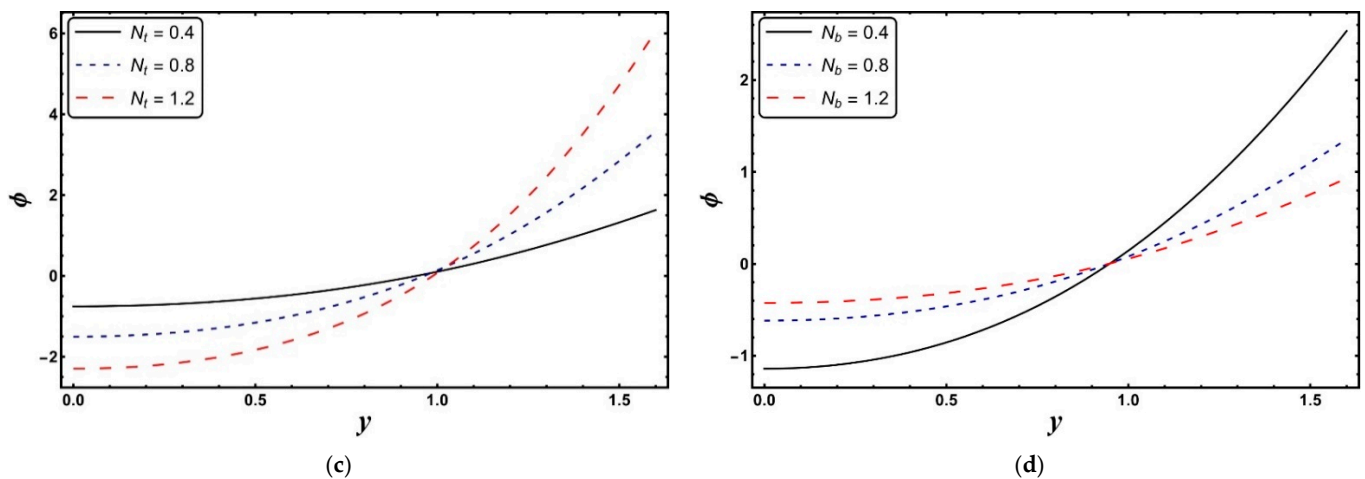


Figure 6. (a–d): Effects of different parameters on concentration profile.

4.6. Rate of Mass Transfer at the Boundary

Table 1 is arranged to see the behavior of various parameters on mass transfer rate at boundary $\phi'(h)$. This table signifies that $\phi'(h)$ rises by expanding the values of S_c , γ and N_t whereas it shows decreasing behavior by increasing N_b .

Table 1. Mass transfer rate at the channel wall against different flow parameters.

S_c	γ_c	N_b	N_t	$\phi'(h)$
0.1	1.0	0.03	0.5	3.6417
0.2				4.1224
0.3				4.7646
0.2	0.0			3.2667
	0.5			3.6417
	1.0			4.1224
		0.1		21.3819
		0.2		9.8702
		0.3		6.6527
			0.1	0.7094
			0.2	1.4692
			0.3	2.2861

4.7. Velocity Profile

Figure 7a–e are sketched to investigate the behavior of Helmholtz Smoluchowski velocity/electroosmotic velocity (U_{hs}), electroosmotic parameter (ω), variable viscosity parameter (α), Hartman number (M) and concentration Grashof number (G_c) on velocity profile. According to Figure 7a, a higher U_{hs} causes a decline in velocity in the middle of channel, while the reverse trend is observed at the boundaries. A positively oriented external electric field can be obtained when U_{hs} is negative. The reverse axial electric field can be archived when U_{hs} is positive, and there is no electric field when $U_{hs} = 0$. For negative U_{hs} , the electroosmotic velocity adds to the peristaltic motion’s velocity, increasing the final axial velocity. The only source of fluid acceleration when $U_{hs} = 0$ is peristalsis, so the velocity is significantly lower than it would be for negative values. However, at positive values, the electroosmotic velocity opposes peristaltic pumping; as a result, the least acceleration of the liquid is observed in this situation. As a result, the direction inside the channel and the electric field’s direction plays a crucial role in determining the characteristics of the velocity distribution. Figure 7b shows that the nanofluid flow increases with increasing electroosmotic parameter. A higher value of the electroosmotic parameter indicates the presence of a higher concentration of ions (in the base fluid), which is responsible for the formation of a thinner EDL layer, thereby creating a lower

velocity resistance force, and hence the fluid flow is increased. It is necessary to state that the magnetohydrodynamic body force is inferior to the electrokinetic effect in terms of hydrodynamic control, and this is crucial for the precise design of micropumps. From Figure 7c, an increment in α yields to an increase in nanofluid velocity. This means that the nanofluid has a higher velocity near the middle of the channel than a nanoliquid with a constant viscosity ($\alpha = 0$) depending on the temperature. Strengthening the viscosity parameter α lowers the viscosity of the nanofluid and therefore resistance to flow, which enhances the nanofluid velocity. A stronger magnetic field results in a lower velocity (see Figure 7d). This is due to the emergence of Lorentz forces. Such trends have been reported in Abbasi et al. [11]. Figure 7e elucidates that velocity retards by increasing the values of G_c . This is primarily because with an increase in G_c the viscosity of nanoliquid increases which lessens the movement of nanoliquid.

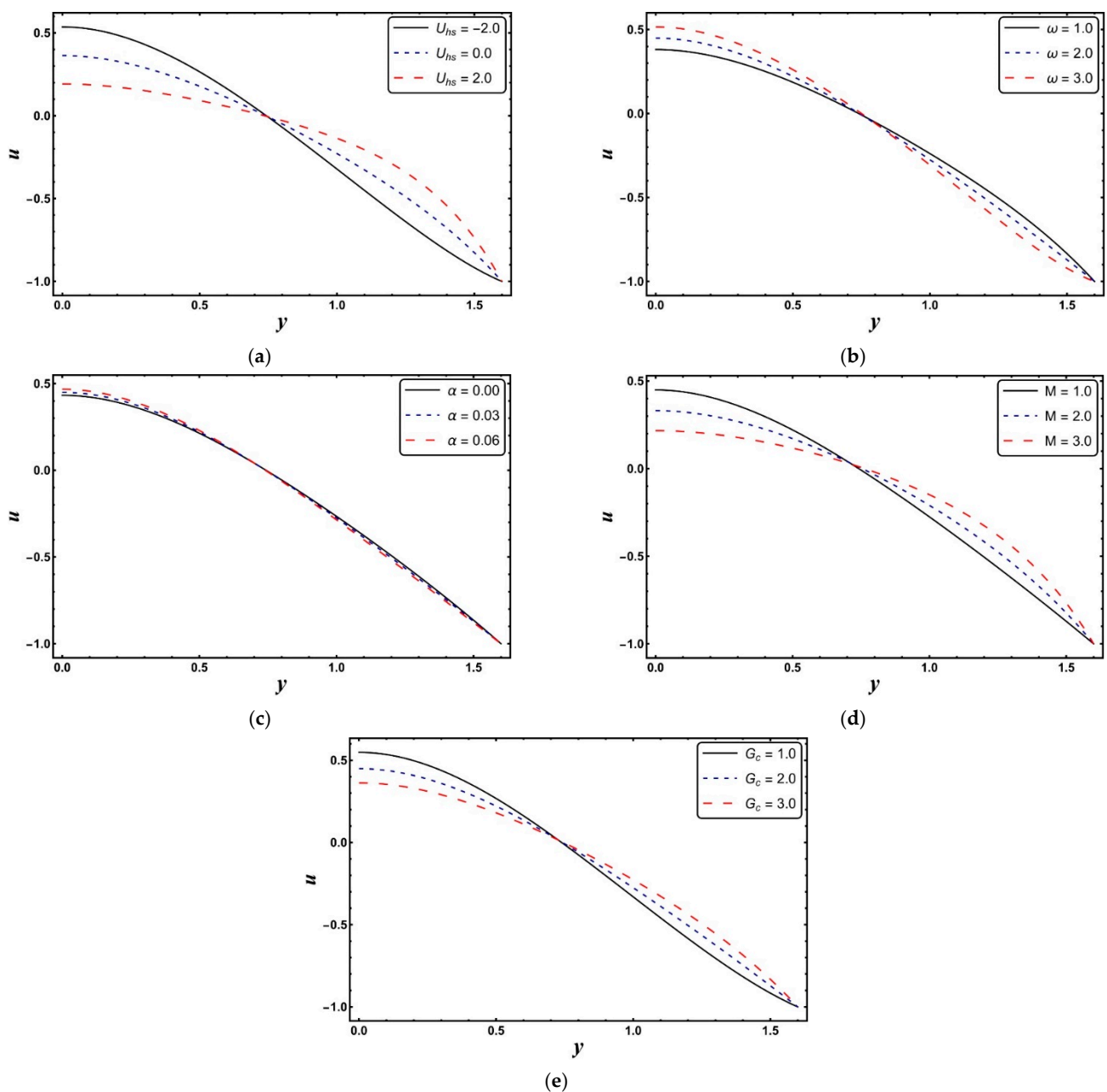


Figure 7. (a–e): Effects of different pertinent parameters on velocity profile.

5. Conclusions

The present study examines the interaction of variable fluid properties with electrokinetically regulated peristaltic transportation of a reactive nanofluid embedded in a porous space. The ensuing key facts have been produced from the above investigation:

- More energy is contributed to the nanofluid system in response of the Joule heating parameter.
- An inclining change in heat transfer rate at the wall associated with the larger Electroosmotic parameter is exhibited.
- It is noticed that the temperature of water is comparatively lower than that of kerosene.
- Entropy generation suppresses for higher variable thermal conductivity parameter.
- The process of irreversibility is even more intensified in the presence of mixed convection.
- The magnitude of Bejan number is enhanced by increasing electroosmotic parameter.
- A substantial decrease in nanoparticles concentration is perceived when chemical reaction parameter is being augmented.
- A significant increase in mass transfer rate at the wall is found at a higher Schmidt number.
- A positively oriented external electric field contributes to the velocity of nanofluid.

Author Contributions: Conceptualization, S.H.; Methodology, Y.A. and H.A.; Software, H.A.; Validation, H.A.; Formal analysis, Y.A.; Investigation, Y.A.; Resources, S.H.; Writing—original draft, Y.A. and H.A.; Writing—review & editing, S.H.; Supervision, S.H.; Project administration, S.H.; Funding acquisition, H.A. All authors have read and agreed to the published version of the manuscript.”

Funding: This research received no external funding.

Data Availability Statement: Not applicable.

Acknowledgments: H. Alotaibi is thankful for the Taif University research supporting project number (TURSP-2020/304), Taif University, Taif, Saudi Arabia.

Conflicts of Interest: The authors declare no conflict of interest.

Nomenclature

(\vec{x}, \vec{y}) :	Coordinates in wave frame
(\vec{U}, \vec{V}) :	Velocity components in lab frame
(\vec{u}, \vec{v}) :	Velocity components in wave frame
n_0 :	Concentration of ions at the bulk
e :	Electronic charge
c :	Speed of peristaltic wave
\vec{J} :	Current density
\vec{B} :	Applied magnetic field
K_B :	Boltzmann constant
\vec{E} :	Applied electric field
C_f :	Specific heat of fluid
μ_f :	Viscosity of fluid
T :	Dimensional temperature
δ :	Wave number
z :	Charge balance
σ_f :	Electric conductivity of fluid
g :	Acceleration due to gravity
(\vec{X}, \vec{Y}) :	Coordinates in lab frame
P :	Dimensional pressure
T_w :	Temperature at channel wall
p :	Dimensionless pressure

T_0 :	Temperature of wall
F :	Dimensionless flow rate in wave frame
θ :	Dimensionless temperature
ψ :	Stream function
η :	Dimensionless flow rate in laboratory frame
Pr :	Prandtl number
K_f :	Thermal conductivity of fluid
Re :	Reynolds number
Br :	Brinkman number
T_{av} :	Average temperature of the electrolytic solution
Ec :	Eckert number
ρ_f :	Density of fluid
G_t :	Temperature Grashoff number
M :	Hartman number
λ :	Wavelength
d_1 :	Half width of the channel
n^+ and n^- :	Number of densities of cations and anions

References

- Latham, T.W. Fluid Motions in a Peristaltic Pump. Master's Thesis, Massachusetts Institute of Technology, Cambridge, MA, USA, 1966.
- Shapiro, A.H.; Jaffrin, M.Y.; Weinberg, S.L. Peristaltic pumping with long wavelengths at low Reynolds number. *J. Fluid Mech.* **1969**, *37*, 799–825. [[CrossRef](#)]
- Srinivas, S.; Gayathri, R.; Kothandapani, M. The influence of slip conditions, wall properties and heat transfer on MHD peristaltic transport. *Comput. Phys. Commun.* **2009**, *180*, 2115–2122. [[CrossRef](#)]
- Khan, A.A.; Usman, H.; Vafai, K.; Ellahi, R. Study of peristaltic flow of magnetohydrodynamics Walter's B fluid with slip and heat transfer. *Sci. Iran.* **2016**, *23*, 2650–2662. [[CrossRef](#)]
- Tanveer, A.; Khan, M.; Salahuddin, T.; Malik, M.Y.; Khan, F. Theoretical investigation of peristaltic activity in MHD based blood flow of non-Newtonian material. *Comput. Methods Programs Biomed.* **2020**, *187*, 105225. [[CrossRef](#)] [[PubMed](#)]
- Choi, S.U.; Eastman, J.A. *Enhancing Thermal Conductivity of Fluids with Nanoparticles*; (No. ANL/MSD/CP-84938; CONF-951135-29); Argonne National Lab (ANL): Argonne, IL, USA, 1995.
- Eastman, J.A.; Choi, U.S.; Li, S.; Thompson, L.J.; Lee, S. Enhanced thermal conductivity through the development of nanofluids. *MRS Online Proc. Libr. OPL* **1996**, *457*, 3. [[CrossRef](#)]
- Shehzad, S.A.; Abbasi, F.M.; Hayat, T.; Alsaadi, F. MHD mixed convective peristaltic motion of nanofluid with Joule heating and thermophoresis effects. *PLoS ONE* **2014**, *9*, e111417. [[CrossRef](#)] [[PubMed](#)]
- Prakash, J.; Sharma, A.; Tripathi, D. Convective heat transfer and double diffusive convection in ionic nanofluids flow driven by peristalsis and electromagnetohydrodynamics. *Pramana* **2020**, *94*, 4. [[CrossRef](#)]
- Eldabe, N.T.; Abouzeid, M.; Shawky, H.A. MHD peristaltic transport of Bingham blood fluid with heat and mass transfer through a non-uniform channel. *J. Adv. Res. Fluid Mech. Therm. Sci.* **2021**, *77*, 145–159. [[CrossRef](#)]
- Abbasi, F.M.; Hayat, T.; Alsaadi, F.; Dobai, A.M.; Gao, H. MHD peristaltic transport of spherical and cylindrical magneto-nanoparticles suspended in water. *AIP Adv.* **2015**, *5*, 077104. [[CrossRef](#)]
- Sajid, T.; Tanveer, S.; Munsab, M.; Sabir, Z. Impact of oxytactic microorganisms and variable species diffusivity on blood-gold Reiner–Philippoff nanofluid. *Appl. Nanosci.* **2021**, *11*, 321–333. [[CrossRef](#)]
- Gasmi, H.; Khan, U.; Zaib, A.; Ishak, A.; Eldin, S.M.; Raizah, Z. Analysis of Mixed Convection on Two-Phase Nanofluid Flow Past a Vertical Plate in Brinkman-Extended Darcy Porous Medium with Nield Conditions. *Mathematics* **2022**, *10*, 3918. [[CrossRef](#)]
- Darcy, H. *Les Fontaines Publiques de la Volle de Dijon*; Vector Dalmont: Paris, France, 1856.
- Alazmi, K.; Vafai, K. Analysis of variants within the porous transport models. *J. Heat Transf.* **2004**, *122*, 303–326. [[CrossRef](#)]
- Alazmi, K.; Vafai, K. Analysis of variable porosity, thermal dispersion and local thermal non-equilibrium on free surface flows through porous media. *J. Heat Transf.* **2004**, *126*, 389–399. [[CrossRef](#)]
- Pal, D.; Mondal, H. Radiation effects on combined convection over a vertical flat plate embedded in a porous medium of variable porosity. *Meccanica* **2009**, *44*, 133–144. [[CrossRef](#)]
- Kuznetsov, A.V.; Nield, D.A. The Cheng–Minkowycz problem for natural convective boundary layer flow in a porous medium saturated by a nanofluid: A revised model. *Int. J. Heat Mass Transf.* **2013**, *65*, 682–685. [[CrossRef](#)]
- Asghar, Z.; Ali, N. Mixed convective heat transfer analysis for the peristaltic transport of viscoplastic fluid: Perturbation and numerical study. *AIP Adv.* **2019**, *9*, 095001. [[CrossRef](#)]
- Rice, C.L.; Whitehead, R. Electrokinetic flow in a narrow cylindrical capillary. *J. Phys. Chem.* **1965**, *69*, 4017–4024. [[CrossRef](#)]
- Tang, G.H.; Li, X.F.; He, Y.L.; Tao, W.Q. Electroosmotic flow of non-Newtonian fluid in microchannels. *J. Non-Newton. Fluid Mech.* **2009**, *157*, 133–137. [[CrossRef](#)]

22. Akbar, Y.; Alotaibi, H. Electroosmosis-Optimized Thermal Model for Peristaltic Transportation of Thermally Radiative Magnetized Liquid with Nonlinear Convection. *Entropy* **2022**, *24*, 530. [[CrossRef](#)]
23. Siryk, S.V.; Bendandi, A.; Diaspro, A.; Rocchia, W. Charged dielectric spheres interacting in electrolytic solution: A linearized Poisson–Boltzmann equation model. *J. Chem. Phys.* **2021**, *155*, 114114. [[CrossRef](#)]
24. Obolensky, O.I.; Doerr, T.P.; Yu, Y.K. Rigorous treatment of pairwise and many-body electrostatic interactions among dielectric spheres at the Debye–Hückel level. *Eur. Phys. J. E* **2021**, *44*, 129. [[CrossRef](#)] [[PubMed](#)]
25. Hussain, A.; Wang, J.; Akbar, Y.; Shah, R. Enhanced thermal effectiveness for electroosmosis modulated peristaltic flow of modified hybrid nanofluid with chemical reactions. *Sci. Rep.* **2022**, *12*, 13756. [[CrossRef](#)] [[PubMed](#)]
26. Bejan, A. A study of entropy generation in fundamental convective heat transfer. *ASME J. Heat Transf.* **1979**, *101*, 718–725. [[CrossRef](#)]
27. Rashidi, M.; Bhatti, M.; Abbas, M.; Ali, M. Entropy generation on MHD blood flow of nanofluid due to peristaltic waves. *Entropy* **2016**, *18*, 117. [[CrossRef](#)]
28. Akbar, Y.; Shanakhat, I.; Abbasi, F.M.; Shehzad, S.A. Entropy generation analysis for radiative peristaltic motion of silver-water nanomaterial with temperature dependent heat sink/source. *Phys. Scr.* **2020**, *95*, 115201. [[CrossRef](#)]
29. Akbar, Y.; Abbasi, F.M. Impact of variable viscosity on peristaltic motion with entropy generation. *Int. Commun. Heat Mass Transf.* **2020**, *118*, 104826. [[CrossRef](#)]
30. Sneha, K.N.; Mahabaleshwar, U.S.; Sharifpur, M.; Ahmadi, M.H.; Al-Bahrani, M. Entropy Analysis in MHD CNTS Flow Due to a Stretching Surface with Thermal Radiation and Heat Source/Sink. *Mathematics* **2022**, *10*, 3404. [[CrossRef](#)]
31. Akbar, Y.; Huang, S. Enhanced Thermal Effectiveness for Electrokinetically Driven Peristaltic Flow of Motile Gyrotactic Microorganisms in a Thermally Radiative Powell Eyring Nanofluid Flow with Mass Transfer. *Chem. Phys. Lett.* **2022**, *808*, 140120. [[CrossRef](#)]